OPEN ACCESS

Microbiology REPORT

Dual-dynamic control and metabolic rebalancing guided by toxic target discovery for efficient dencichine production

Yu Zhang,[1] Jun Wu,[1] Jinghua Yu,[1] Yong Tang,[1] Chong Xie,[1] Xiaolin Shen,[1] Jia Wang,[1] Yajun Yan,[2] Xinxiao Sun,[1,*] and Qipeng Yuan[1,*]

*Correspondence: sunxx@mail.buct.edu.cn (S.X.); yuanqp@mail.buct.edu.cn (Y.Q.)

Received: March 6, 2026; Accepted: August 17, 2026; Published Online: August 18, 2026; https://doi.org/10.59717/j.xinn-life.2026.100242

GRAPHICAL ABSTRACT

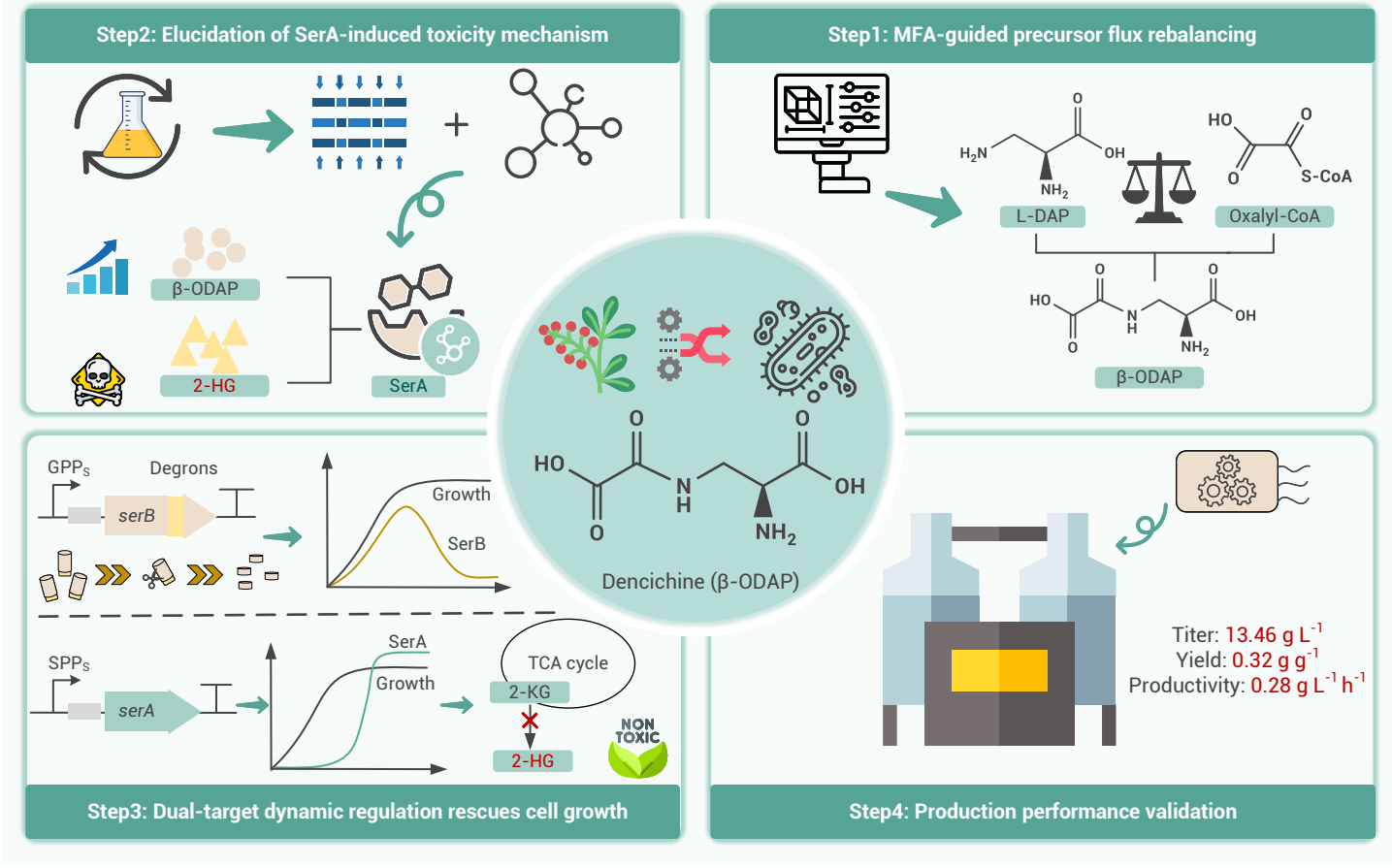

PUBLIC SUMMARY

- Elucidating the toxicity mechanism caused by overexpressing *serA* encoding 3-phosphoglycerate dehydrogenase.
- Engineering a dual-dynamic genetic circuit to improve cell growth and dencichine (β-ODAP) production.
- This systematic engineering strategy enables the highest reported biosynthesis titer of β-ODAP.

REPORT Microbiology

OPEN ACCESS

Dual-dynamic control and metabolic rebalancing guided by toxic target discovery for efficient dencichine production

Yu Zhang,[1] Jun Wu,[1] Jinghua Yu,[1] Yong Tang,[1] Chong Xie,[1] Xiaolin Shen,[1] Jia Wang,[1] Yajun Yan,[2] Xinxiao Sun,[1,*] and Qipeng Yuan[1,*]

[1]State Key Laboratory of Chemical Resource Engineering, Beijing University of Chemical Technology, Beijing 100029, China

[2]School of Chemical, Materials and Biomedical Engineering, College of Engineering, The University of Georgia, Athens GA 30602, USA

*Correspondence: sunxx@mail.buct.edu.cn (S.X.); yuanqp@mail.buct.edu.cn (Y.Q.)

Received: March 6, 2026; Accepted: August 17, 2026; Published Online: August 18, 2026; https://doi.org/10.59717/j.xinn-life.2026.100242

Citation: Zhang Y., Wu J., Yu J., et al. (2026). Dual-dynamic control and metabolic rebalancing guided by toxic target discovery for efficient dencichine production. *The Innovation Life* **4**:100242.

Construction of microbial cell factories often requires extensive reconfiguration of metabolic networks, which frequently compromises cell growth. Here, we engineered *E. coli* to produce dencichine (β-ODAP), a plant-derived hemostatic agent. Knocking out *serB* blocks the competing *L*-serine pathway, causing *L*-serine auxotrophy and severely impairing cell growth. This growth defect was only partially restored by supplementation with *L*-serine or *L*-glycine, suggesting the presence of additional growth-limiting factors. Through adaptive laboratory evolution and reverse engineering, we further uncovered that overexpression of *serA* to enhance the supply of the precursor *L*-2,3-diaminopropionate led to accumulation of the toxic byproduct 2-hydroxyglutarate (2-HG) from α-ketoglutarate. To resolve these two growth constraints, we developed a growth-phase-dependent dual-dynamic regulation circuit. This circuit gradually activates *serA* expression and progressively represses *serB* expression as cells enter the stationary phase, thereby reducing 2-HG accumulation and alleviating *L*-serine auxotrophy. Combined with pathway balancing and cofactor optimization, the final engineered strain produced 13.46 g L^{-1} of β-ODAP with a yield of 0.32 g g^{-1} in 3-L bioreactors. This study reveals a toxicity mechanism in serine-pathway engineering and provides a dynamic regulation strategy applicable to the biosynthesis of serine-pathway-derived metabolites.

INTRODUCTION

Microbial synthesis offers a green and sustainable route for producing natural products, yet its industrial applicability is often constrained by low biosynthetic efficiency.[1–6] The major bottlenecks include the metabolic burden imposed by heterologous pathways,[7,8] the accumulation of toxic intermediates or byproducts,[9] and the inherent trade-off between cell growth and product synthesis.[10] These challenges continue to limit the performance of engineered strains, highlighting the need for a deeper understanding of host metabolism and the development of corresponding regulation strategies.

To achieve efficient production, extensive remodeling of the host metabolic network is typically required, including overexpression of biosynthetic genes and deletion or attenuation of competing pathways. However, such modifications frequently introduce auxotrophies and lead to the accumulation of toxic metabolites, severely compromising cell viability.[11–17] For instance, during the production of artemisinic acid, imbalanced gene expression results in the accumulation of the toxic intermediate 3-hydroxy-3-methylglutaryl coenzyme A (HMG-CoA), a problem later mitigated by protein scaffold-based multi-enzyme assembly.[18] Besides the accumulation of toxic metabolites within the engineered pathway, the substrate promiscuity of pathway enzymes can also generate off-pathway toxic metabolites, which are more difficult to identify.[19–22] The *L*-serine biosynthesis pathway, which supplies *L*-serine, *L*-glycine, one-carbon units and other essential metabolites, has proven particularly sensitive to such perturbations. In many engineering attempts, overexpression of the key *L*-serine pathway genes (*serA* or *serABC*), consistently impairs cellular growth, yet the underlying mechanism has remained obscure.[23–26]

To alleviate growth defects caused by metabolic toxicity and auxotrophy, dynamic regulation has emerged as a powerful alternative to static interventions. [27,28] Unlike static control, dynamic regulation allows metabolic fluxes to be autonomously redistributed between growth and production phases, reducing the physiological penalty imposed on the host.[29,30] Various dynamic control systems have been developed, including quorum sensing circuits,[31–33] intermediate or product biosensors,[34,35] and growth-phase-dependent promoters.[36–38] For example, Xu et al. rewired the native FapR regulator to construct malonyl-CoA-responsive sensors that dynamically balance malonyl-CoA supply and consumption, enabling efficient production of malonyl-CoA-derived compounds.[39] Ge et al. engineered a library of quorum sensing variants with high dynamic range and low leakiness, achieving autonomous regulation of multiple fluxes.[32] Notably, growth-phase-dependent promoters offer an additional advantage as they require no heterologous regulatory proteins, thereby minimizing extra metabolic burden.

Dencichine (β-ODAP) is a non-protein amino acid derived from *Panax notoginseng*, exhibiting significant hemostatic activity and neuroprotective effects.[40–42] As a downstream metabolite of the *L*-serine pathway, its biosynthesis is intimately linked to *L*-serine metabolism. In previous work, a heterologous pathway for β-ODAP via the *L*-serine route was established, achieving a titer of 1.29 g L^{-1} in shake flasks, but cell growth was severely compromised.[43] In this study, we uncovered that *serB* deletion caused growth inhibition by *L*-serine auxotrophy while excessive SerA activity redirected α-ketoglutarate toward the toxic byproduct 2-hydroxyglutarate (2-HG), which further suppressed cell growth. To resolve these dual constraints, we designed a growth-coupled dual-dynamic regulation circuit that reciprocally controls *serA* and *serB* expression. Combined with pathway balancing and cofactor optimization, this strategy successfully alleviated metabolic toxicity, restored cell growth, and enabled efficient β-ODAP production. Collectively, our work resolves a toxicity puzzle in serine-pathway engineering and provides a practical dynamic regulation strategy that can be extended to the biosynthesis of other serine-derived metabolites.

MATERIALS AND METHODS

Genetic manipulation

Strains and plasmids used in this study are listed in Table S1 and Table S2, respectively. Promoter and degron sequences were listed in Table S4 and Table S5, respectively. The plasmid was constructed by homologous recombination using the pEASY®-Basic Seamless Cloning and Assembly Kit. Genomic modifications were performed using CRISPR/Cas9 as previously described.[44] The details of genetic manipulations were described in Supplementary Note 1.

Metabolic flux analysis

The latest *E. coli* model ec_iML1515 was extended by introducing exogenous reactions to generate β-ODAP-specific models for different artificial pathways and the theoretical yields were compared (Figure S1). To simulate flux distribution, flux balance analysis was performed using the oxaloacetate cleavage model constrained by experimentally determined production rates and glycerol consumption rates (Figure S2) with the objective function of biomass maximization (Figure S3). The details of metabolic flux analysis were described in Supplementary Note 2.

Adaptive laboratory evolution

Strain DAP6 was cultivated in LB medium for 12 h at 37°C, then the cell suspension was diluted to 1 OD_{600} for ARTP treatment. The ARTP system conditions were listed in Table S6. The lethality curve of the strain DAP6 was shown in Figure S7. Mutagenized cells were subjected to adaptive evolution in MMC system. After 45 passages, droplets 35 with restored growth were

Table 1. Theoretical yields of β-ODAP via different artificial routes.

Different pathways	*L*-DAP modular	Oxalyl-CoA modular	β-ODAP modular	Theoretical yield (mol mol^{-1})
Oxaloacetate cleavage pathway	*SasbnAB*	*Fpoah-ScAAE*	*LsBAHD*	0.531
Glyoxylate Oxidation pathway	*SasbnAB*	*Scgloxdh-ScAAE*	*LsBAHD*	0.416
Synergistic pathway	*SasbnAB*	*Fpoah-Scgloxdh-ScAAE*	*LsBAHD*	0.531

isolated (Figure S8), and 20 larger single colonies were selected for cultivation in shake flasks (Figure S9). Subsequently, three strains with higher cell density, DAP-M8, DAP-M16, and DAP-M19, were subjected to biological replicates in shake flasks, and their genomes were extracted for whole-genome sequencing. The genome sequencing analysis was described in Supplementary Note 3.

Enzyme activity assay of GlpK and SerA

GlpK and its variants activity were determined by measuring ATP consumption using a Kinase Assay Kit (Beyotime, China). SerA and its variants activity were determined by monitoring the decrease in NADH absorbance at 340 nm. The reaction systems are listed in Table S7.

Metabolomics analysis

The strains of DAP6 and DAP-M19 were cultivated in shake flasks until mid-log phase and then centrifuged at 6000 rpm and 4 °C for 10 min. After removing the supernatant, the cell pellets were immediately quenched by immersion in liquid nitrogen for 30 s. Finally, the sample metabolites were analyzed by Tsingke Biotechnology Co., Ltd.

Fluorescence intensity characterization

The *E. coli* transformants were cultured in a deep-well plate containing 1 mL of LB medium at 37°C for 12 h. Then, the above culture was diluted 1:200 and transferred into a microplate with a clear bottom (Corning, NY, USA) containing 200 μL of LB medium with 100 mg L^{-1} ampicillin. Samples were measured using a Synergy HT (BioTek Instruments, VT, USA) microplate reader. The mCherry intensity was detected at an excitation wavelength of 580 nm and an emission wavelength of 620 nm.

NADH/NAD$^+$ measurement

The NADH and NADH/NAD+ measurement was performed following the protocol of the NAD$^+$/NADH Assay Kit (Beyotime, China).

Cultivation in shake flasks

Engineering strains were cultivated in test tubes containing 5 mL LB medium at 37°C and 200 rpm for 10 h. The seed cultures (1 mL) were transferred into 250 mL shake flasks containing 50 mL of M9Y medium and cultivated at 37°C and 200 rpm. The compositions and concentrations of M9Y medium in shake flasks was listed in Table S8. When needed, ampicillin, kanamycin, chloramphenicol and IPTG were supplemented at the beginning of fermentation to the final concentrations of 100 mg L^{-1}, 50 mg L^{-1}, 34 mg L^{-1} and 120 mg L^{-1}, respectively.

Fed-batch fermentation in a 3 L bioreactor

Engineering strains cultured in test tubes (1 mL) were transferred to 100 mL of M9N medium and incubated at 37°C and 200 rpm for 10 h. The seed culture was transferred to 900 mL of M9N medium in a 3 L bioreactor and cultivated at 37°C. The compositions and concentrations of M9N medium was listed in Table S9. During the fermentation process, the pH was maintained at 7.0 using ammonium hydroxide (25%, v/v). When glycerol was exhausted in initial medium, the glycerol solution (50%, w/v) was fed at an appropriate rate. When needed, ampicillin, kanamycin and IPTG were supplemented at the beginning of fermentation to the final concentrations of 100 mg L^{-1}, 50 mg L^{-1} and 120 mg L^{-1}, respectively.

Analytical methods

The cell density was monitored by measuring the absorbance at 600 nm (OD_{600}). *L*-DAP and β-ODAP were analyzed by HPLC using a precolumn derivatization method, as previously described.[43] Oxalate was detected by HPLC with a C18 column at 30°C, using a mobile phase of 0.02 mol L^{-1} KH_2PO_4 and methanol at 0.5 mL min^{-1} (95:5, v/v), and quantified by UV detection at 210 nm. Glycerol, acetate and 2-HG were detected by HPLC equipped with refractive index detector using 5 mM H_2SO_4 as the mobile phase at a flow rate of 0.5 mL min^{-1}.

RESULTS

Evaluating different β-ODAP biosynthesis pathways

In previous study, *de novo* biosynthesis of β-ODAP was achieved by the design of artificial pathways, in which oxalate was generated by either oxaloacetate cleavage (OC) or glyoxylate oxidation (GO).[43] Here, we began by comparing the maximum theoretical yields of these pathways using flux balance analysis (Figure S1 & Table 1). The OC pathway showed a higher theoretical yield (0.531 mol mol^{-1}) compared to the GO pathway (0.416 mol mol^{-1}). In addition, combining the two pathways did not lead to a further increase in the theoretical yield. Therefore, we selected the OC pathway for constructing an efficient microbial cell factory for β-ODAP production.

Furthermore, metabolic flux analysis revealed that the flux toward the *L*-DAP precursor O-phospho-*L*-serine (OPS) was only 0.096 mol mol^{-1}, with 87.5% diverted to *L*-serine biosynthesis. In contrast, the oxalyl-CoA precursor oxaloacetate (OAA) showed a flux 2.5-fold higher than OPS, and the flux of oxalyl-CoA was 8.3 times greater than that of *L*-DAP. This pronounced flux imbalance between the two parallel precursors challenges efficient β-ODAP biosynthesis, as such networks require strict stoichiometric balancing. Moreover, the flux directed to β-ODAP synthesis was only 0.0064 mol mol^{-1}, indicating that the acyltransferase may be a key bottleneck (Figures 1 & S3).

Fine-tuning the flux distribution of multi-nodes to coordinate precursor supply

Given the metabolic flux analysis results, we prioritized enhancing the low-flux *L*-DAP branch via genomic integration. The expression cassette P_{trc}-*SasbnAB* was sequentially integrated into the *E. coli* BW25113 genome, generating strains DAP1, DAP2, and DAP3. Increasing the copy number of *SasbnAB* raised *L*-DAP titers to 0.11, 0.44, and 0.49 g L^{-1}, respectively (Figure 2B). However, the third copy conferred only an 11.4% improvement, indicating that the SbnAB-catalyzed step was no longer the bottleneck. Since *L*-serine competes with *L*-DAP for the common precursor OPS, with most carbon flux directed toward *L*-serine (Figures 1A & S3), we knocked out *serB*. Compared with strain DAP3, the *L*-DAP titer of DAP4 was increased by 2.88-fold to 1.90 g L^{-1}, but due to *L*-serine auxotrophy, the cell density (OD_{600}) was reduced by 74.2% to 4.32 at 60 h (Figure 2B & Table S10). Further introduction of plasmid pZE-*SasbnAB* into DAP4 increased *L*-DAP production by 46.8%, suggesting that *SasbnAB* expression still required enhancement (Figure S4). Thus, a fourth copy of P_{trc}-*SasbnAB* was integrated into the *ilvG* locus of DAP4, yielding strain DAP5, which produced 2.67 g L^{-1} *L*-DAP, comparable to the plasmid-based expression (2.79 g L^{-1}) (Figure 2B). Since only 9.6% of total carbon entered the OPS node (Figures 1A & S3), we enhanced carbon diversion from 3-PG to OPS by integrating P_{trc} driven *serA-serC* into the *yghx* locus of DAP5. The resulting strain DAP6 produced 3.07 g L^{-1} *L*-DAP, a 15.0% increase over DAP5 (Figure 2B).

Next, we introduced plasmid pCS-*Ls*BAHD-*Sc*AAE-*Fp*Oah into strain DAP6 to produce β-ODAP. However, the resulting strain ODAP1 produced only 0.26 g L^{-1} of β-ODAP, with substantial *L*-DAP accumulation (2.78 g L^{-1}) (Figure 2C). We considered two possible limitations: inadequate supply of oxalyl-CoA, or imbalanced expression of the three pathway genes. Supplementation with OAA, pantothenate (a CoA precursor), or both, failed to improve β-ODAP production (Figure S5), suggesting that oxalyl-CoA synthesis was not limited by substrate availability.

Modular pathway engineering was then employed to optimize gene

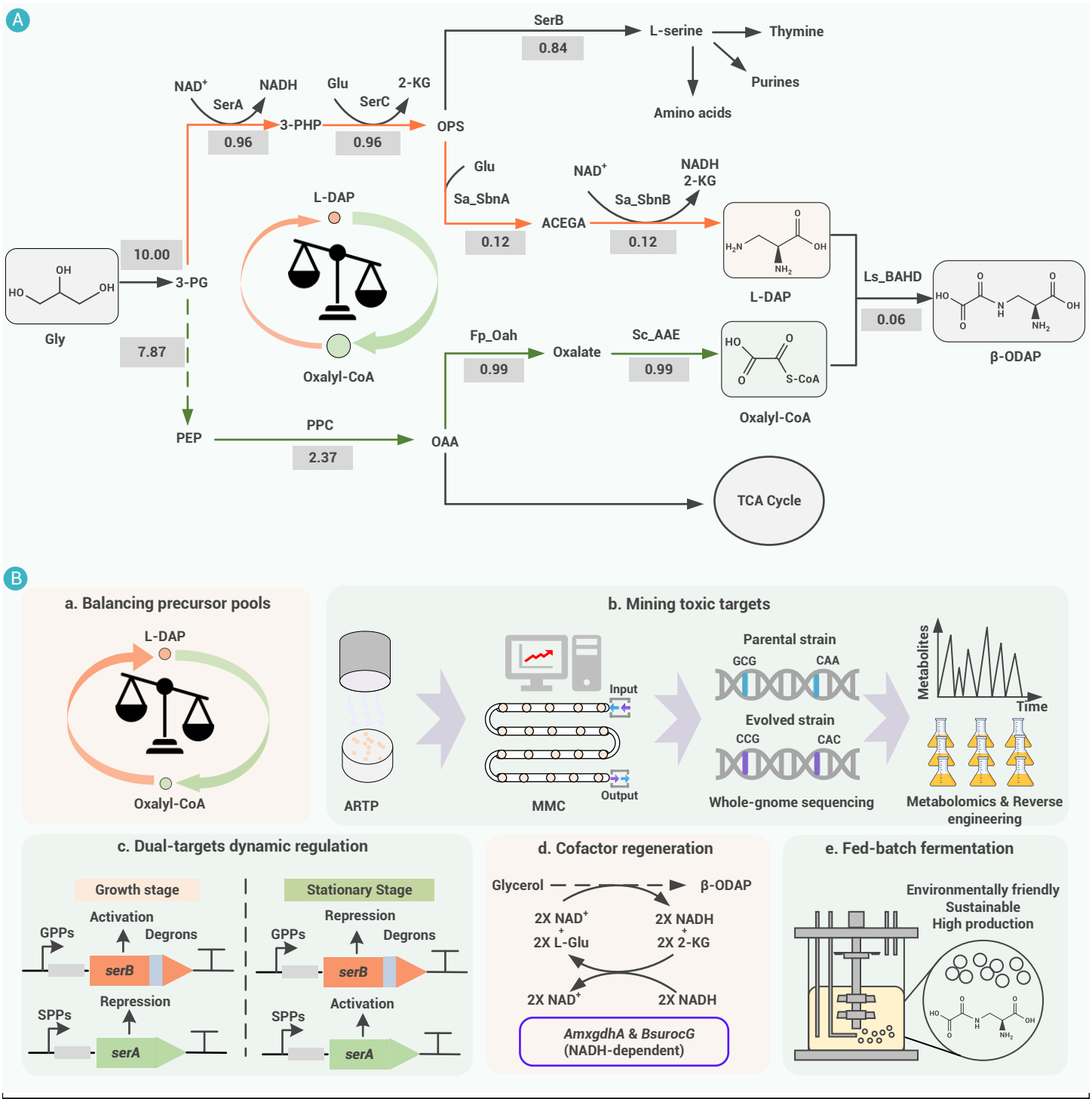

Figure 1. Schematic diagram of engineered *E. coli* for high-level production of β-ODAP (A) Metabolic flux analysis of oxaloacetate cleavage pathway. (B) The overview of strategies for β-ODAP biosynthesis in *E. coli*. β-ODAP, dencichine; 2-KG, α-ketoglutarate; 3-PG, 3-phosphoglycerate; 3-PHP, 3-phosphooxypyruvate; ACEGA, N-(2S)-2-amino-2-carboxyethyl-L-glutamate; Gly, glycerol; *L*-DAP, *L*-2,3-diaminopropionate; *L*-Ser, *L*-serine; OAA, oxaloacetate; OPS, O-phospho-*L*-serine; PEP, phosphoenolpyruvate; SerA, 3-phosphoglycerate dehydrogenase; SerC, phosphoserine aminotransferase; SerB, phosphoserine phosphatase; PPC, phosphoenolpyruvate carboxylase; *Sa*_SbnA, N-(2S)-2-amino-2-carboxyethyl-L-glutamate synthase from *Staphylococcus aureus*; *Sa*_SbnB, N-(2S)-2-amino-2-carboxyethyl-L-glutamate dehydrogenase from *Staphylococcus aureus*; *Fp*_Oah, oxaloacetate hydrolase from *Fomitopsis palustris*; *Sc*_AAE, acyl-activating enzyme from *Saccharomyces cerevisiae*; *Ls*_BAHD, BAHD acyl transferase from *Lathyrus sativus*.

expression. As the direct interaction of acyl-activating enzyme AAE and the acyltransferase BAHD,[45] they were expressed as one module (the AB module) while *Fp*Oah as another (Oxalate module) (Figure 2A). The results showed that the oxalate module performed best on a medium-copy plasmid, while the AB module was more effective on a high-copy plasmid. The best strain ODAP3 (DAP6 carrying pZE-*Ls*BAHD-*Sc*AAE and pCS-*Fp*Oah) produced 0.61 g L^{-1} β-ODAP, accumulated 2.47 g L^{-1} *L*-DAP, and showed a 20.5% decrease in cell density. Conversely, high-copy expression of the oxalate module (strains ODAP2 and ODAP4) reduced both cell growth (by 36.7%-40.5%) and L-DAP production (by 39.6-96.4%), indicating that excessive oxaloacetate hydrolysis not only impaired TCA flux, but also interfered with *L*-DAP synthesis (Figure 2C). Considering the cell growth burden, we further optimized the AB module using promoters engineering ($P_{lpp0.2}$ [low], $P_{lpp0.6}$ [medium], $P_{lpp1.2}$ [high]). *LsBAHD* performed better under weaker promoter whereas *ScAAE* benefited from stronger promoters. The optimal strain ODAP11 (DAP6 carrying pZE-$P_{lpp0.2}$-*Ls*BAHD-$P_{lpp1.2}$-*Sc*AAE and pCS-*Fp*Oah)

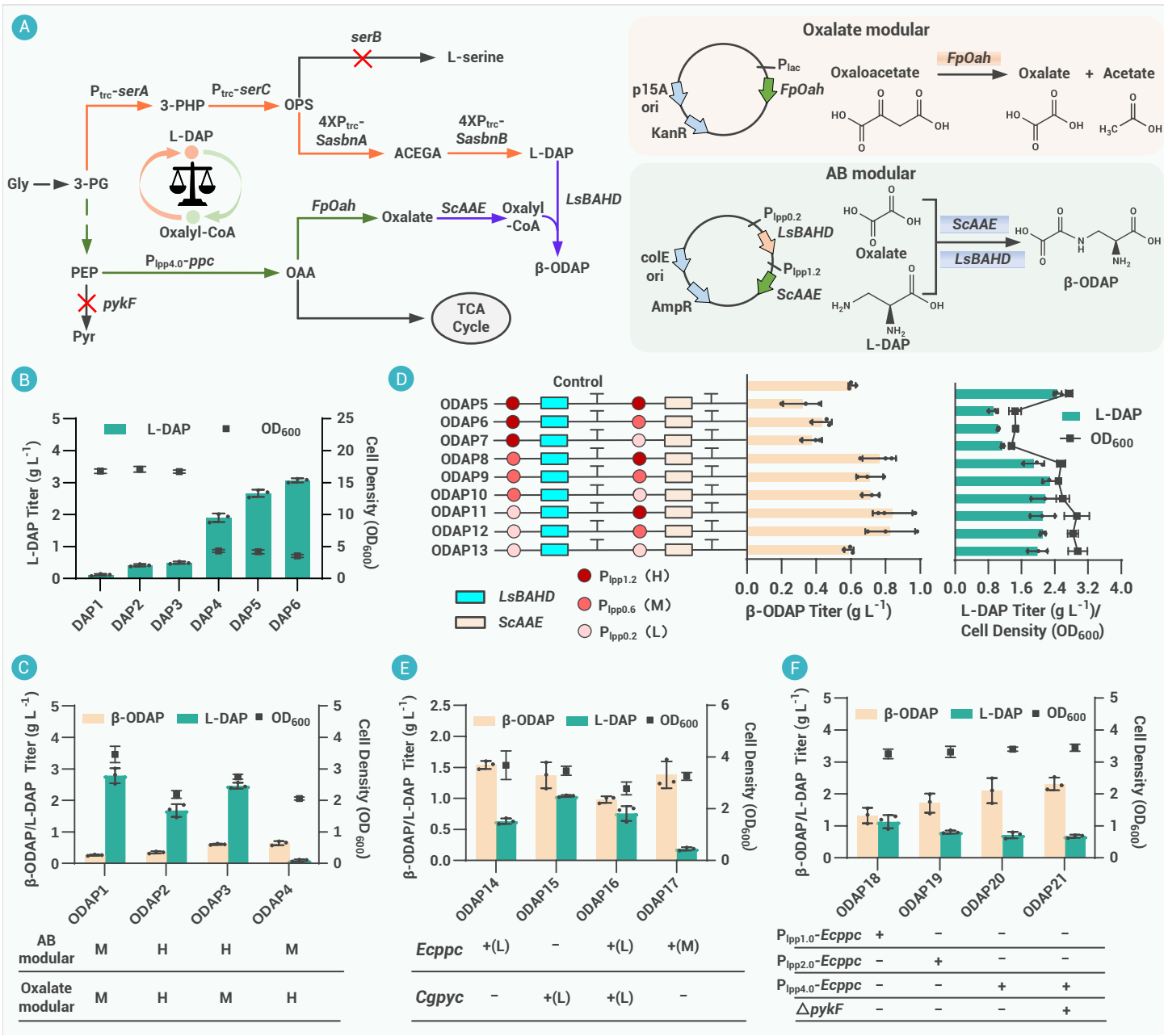

Figure 2. Enhancing and balancing the supply of precursors *L*-DAP and oxalyl-CoA (A) Schematic overview of the modifications of two parallel biosynthetic pathways. (B) Stepwise improvement in *L*-DAP titers through metabolic engineering in the *E. coli* genome. (C) Optimizing the oxalate and AB module to enhance β-ODAP production. M, medium-copy plasmid (pCS27); H, high-copy plasmid (pZE12-luc). (D) Balancing the expression of *LsBAHD* and *ScAAE* by promoter engineering in pZE12-luc. (E) Increasing oxalyl-CoA supply through diverse oxaloacetate anaplerotic pathways. M, medium-copy plasmid (pCS27); L, low-copy plasmid (pSA74). (F) Increasing the β-ODAP titer by optimizing *ppc* expression at the *ycgh* locus and knocking out *pykF* in strain ODAP11 (DAP6 carrying pZE-$P_{lpp0.2}$-*Ls*BAHD-$P_{lpp1.2}$-*Sc*AAE and pCS-*Fp*Oah). Data shown are the mean of n=3 biologically independent experiments and error bars represent standard deviation.

produced 0.84 g L^{-1} β-ODAP, a 37.7% increase over ODAP3, with a 6.5% improvement in biomass (Figure 2D). Overall, multi-round optimization of the AB module increased β-ODAP titers by 223.1%, confirming that imbalanced expression of *LsBAHD* and *ScAAE* had limited production.

To further increase β-ODAP output, we targeted oxaloacetate supply by overexpressing *ppc* (from *E. coli*) or *pyc* (from *C. glutamicum*) via a low-copy plasmid. Overexpression of *ppc* from a low-copy plasmid in strain ODAP14 yielded the highest β-ODAP production (1.54 g L^{-1}) with 0.63 g L^{-1} *L*-DAP accumulation, whereas using a medium-copy plasmid (strain ODAP17) failed to improve β-ODAP and further reduced *L*-DAP to 0.19 g L^{-1} (Figure 2E). This result was consistent with the unexpected decrease in *L*-DAP accumulation caused by overexpression of *Fpoah* from a high-copy plasmid (Figure 2C). These findings indicated that enhancing *ppc* and *Fpoah* promoted the supply of oxalyl-CoA, thereby facilitating the conversion of *L*-DAP to β-ODAP. However, due to competition between the two precursors and the reversibility of the SerA- and SerC- catalyzed reaction, excessive elevation of oxalyl-CoA flux ultimately restricted *L*-DAP synthesis. We therefore fine-tuned *ppc* expression in the *ycgh* locus of ODAP11 using promoters of varying strengths ($P_{lpp1.0}$, $P_{lpp2.0}$, $P_{lpp4.0}$, from weak to strong). The best strain, ODAP20, produced 2.10 g L^{-1} β-ODAP, a 150% increase over ODAP11, with 0.71 g L^{-1} *L*-DAP (Figure 2F). Knocking out *pykF* to increase PEP availability slightly improved β-ODAP titer to 2.31 g L^{-1} in ODAP21, with 0.67 g L^{-1} *L*-DAP (Figure 2F). Despite these improvements, all engineered strains based on DAP6 showed severe growth defects. Supplementation with *L*-serine or *L*-glycine could not restore growth to wild-type levels (Figure S6), suggesting the presence of unidentified metabolic dysregulation.

Unraveling the toxicity mechanism of DAP6 through ALE

To identify targets affecting growth, DAP6 was subjected to atmospheric room temperature plasma (ARTP) mutagenesis followed by adaptive evolu-

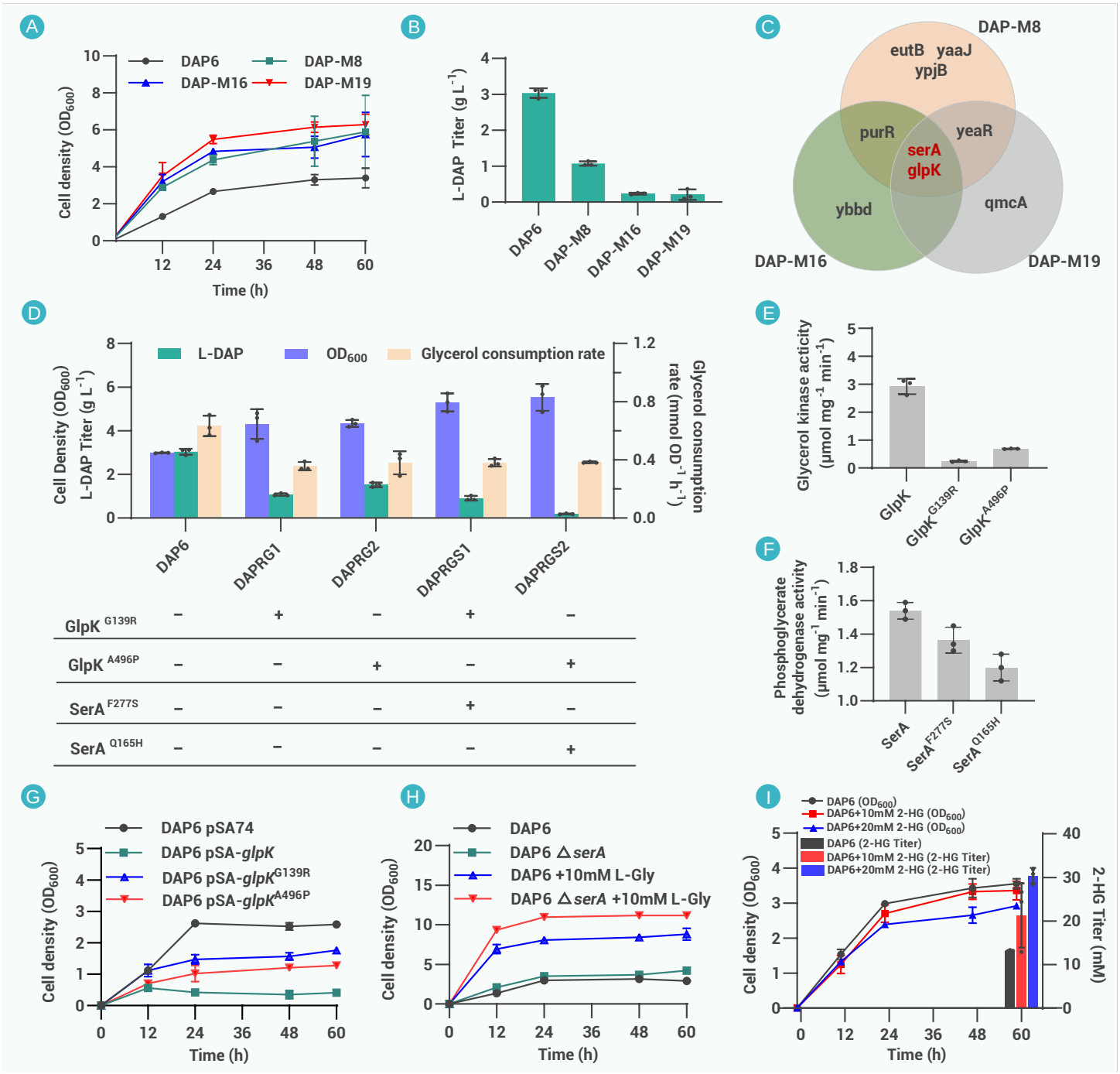

Figure 3. Toxicity target identification via ALE of DAP6 Comparison of cell growth (A) and *L*-DAP production (B) between DAP6 and the evolved strains. (C) Mutations identified in three evolved strains via whole-genome sequencing. (D) Reverse engineering validates the effects of GlpK and SerA mutants on cell growth, glycerol consumption, and L-DAP titers. (E) In vitro enzyme activity assay of GlpK, GlpK^{G139R} and GlpK^{A496P}. (F) In vitro enzyme activity assay of SerA, SerA^{F277S} and SerA^{Q165H}. (G) Growth curves of strains overexpressing *glpK*, *glpK*^{G139R} and *glpK*^{A496P} in low-copy-number plasmids. (H) Growth curves of DAP6 and DAP6 Δ*serA* with or without L-glycine supplementation. (I) Toxicity verification of 2-hydroxyglutarate. Data shown are the mean of n=3 biologically independent experiments and error bars represent standard deviation.

tion in a microbial microdroplet culture (MMC) system. After 45 passages, microdroplet 35 exhibited the highest cell density (Figure S8). Among twenty monoclonal isolates from this droplet, most showed improved growth but reduced *L*-DAP production (Figure S9). Three evolved strains with high cell density—DAP-M8, DAP-M16, and DAP-M19—were selected for whole-genome sequencing (Figures 3A-B). We identified eight single-nucleotide variations (SNVs) and one insertion, with nonsynonymous mutations in *glpK* and the overexpressed *serA* gene common to all evolved strains (Table S3 & Figure 3C). These mutations were further confirmed by Sanger sequencing.

Reverse engineering was used to validate the contributions of these mutations to cell growth. Introducing *glpK*^{G139R} and *glpK*^{A496P} into DAP6 yielded strains DAPRG1 and DAPRG2, which increased cell density by 44.1% and 44.8%, respectively, but significantly reduced glycerol consumption (64.7% and 50.1%) and *L*-DAP production (43.7% and 40.0%) (Figure 3D). Enzyme assays confirmed that both GlpK^{G139R} and GlpK^{A496P} had reduced activity (0.25 and 0.69 μmol mg^{-1} min^{-1}, respectively) compared to the wild type (2.92 μmol mg^{-1} min^{-1}) (Figure 3E & S10). Compared to strain DAP6, overexpression of wild-type or mutant *glpK* further inhibited growth, though mutants were less detrimental (Figure 3G), suggesting that attenuated glycerol metabolism helped avoid toxic intermediate accumulation.

We next introduced the *serA* mutations into the *glpK*-mutant backgrounds. Strains DAPRGS1 (*glpK*^{G139R}*serA*^{F277S}) and DAPRGS2 (*glpK*^{A496P}*serA*^{Q165H}) showed additional improvements in cell density (23.0% and 27.7%, respectively), but *L*-DAP production dropped to 0.91 g L^{-1} and 0.19 g L^{-1} (Figure 3D).

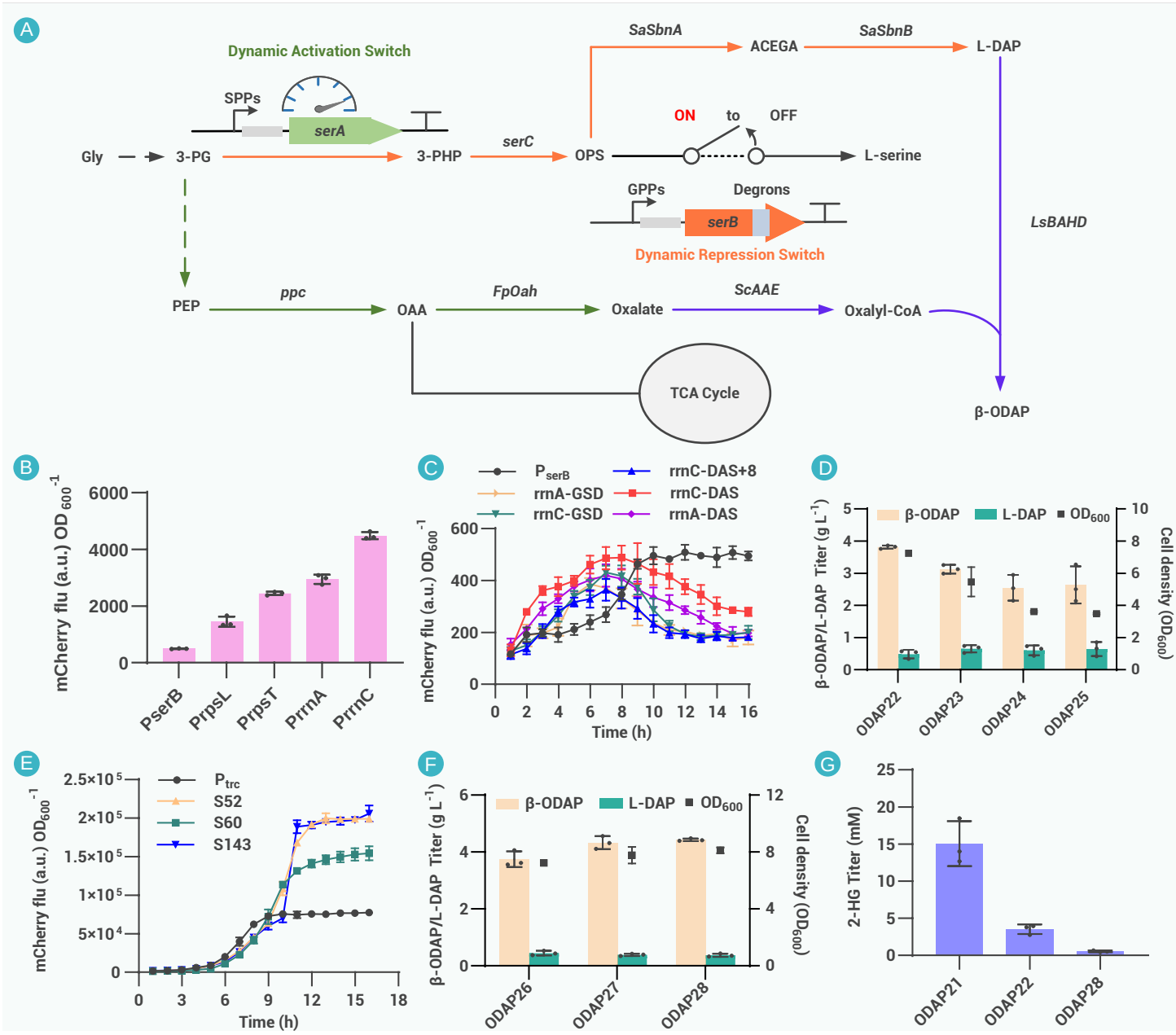

Figure 4. Dynamic regulation of growth-related targets via bifunctional genetic switch (A) Schematic diagram showing dynamic activation and repression switches that respectively regulate *serA* and *serB* expression. (B) Comparison of the strength of the native *serB* promoter and GPPs using mCherry-specific fluorescence. (C) The fluorescence curves of five typical GPPs-degrons combinations. (D) Improving β-ODAP titers and cell growth by dynamically repressing *serB* expression. (E) The fluorescence curves of P_{trc} and SPPs using mCherry-specific fluorescence. (F) Improving β-ODAP titers and cell growth by dynamically activating *serA* expression. (G) 2-HG accumulation in the fermentation broth of ODAP21, ODAP22, and ODAP28. Data shown are the mean of n=3 biologically independent experiments and error bars represent standard deviation.

Consistently, enzymatic assays revealed that the activities of $SerA^{F277S}$ (1.36 μmol mg^{-1} min^{-1}) and $SerA^{Q165H}$ (1.20 μmol mg^{-1} min^{-1}) decreased by 11.7% and 22.1%, respectively, compared to the wild type (1.54 μmol mg^{-1} min^{-1}) (Figure 3F & S10). Deleting overexpressed *serA* in DAP6 modestly improved growth, and adding *L*-glycine further enhanced cell density by 42.2% (Figure 3H), confirming that *serA* overexpression impaired growth.

As shown in Figure S11, metabolomic comparison of DAP6 and DAP-M19 revealed decreased levels of central carbon intermediates such as pyruvate, fumarate, and malate, indicating suppressed glycerol metabolism. Levels of *L*-glutamate and γ-aminobutyric acid were elevated, suggesting rerouting of carbon due to reduced *L*-DAP synthesis. Although previous studies reported that the SerA product 3-phosphohydroxypyruvate can be converted into the toxic byproduct 3-hydroxypyruvate,[46,47] its level remained unchanged in the evolved strain DAP-M19. Notably, the level of another toxic byproduct 2-HG, produced by SerA through promiscuous activity on α-ketoglutarate,[21,48] decreased by 78%. In fact, 13 mM of 2-HG was detected during the fermentation of DAP6. Furthermore, adding 2-HG inhibited DAP6 growth in a dose-dependent manner (Figure 3I), confirming its toxicity and underscoring the need to control its accumulation.

Dynamically regulating β-ODAP biosynthesis using bifunctional genetic switches

To address both the *L*-serine auxotrophy caused by *serB* knockout and the accumulation of the toxic byproduct 2-HG resulting from *serA* overexpression, we developed a self-regulated bifunctional genetic circuit that responds to specific cellular physiological states (Figure 4A). We first screened four growth-phase-dependent promoters (GPPs; rpsL, rpsT, rrnA, rrnC) with different strengths, which enable gene expression during the log phase and turn off in the stationary phase,[49] to dynamically attenuate the expression of *serB*. However, all tested GPPs showed higher promoter strength than the native *serB* promoter (Figure 4B). To achieve net downregulation of SerB, four degrons with different degradation rates (DSA, GSD, DSA+8, LAA, ranging

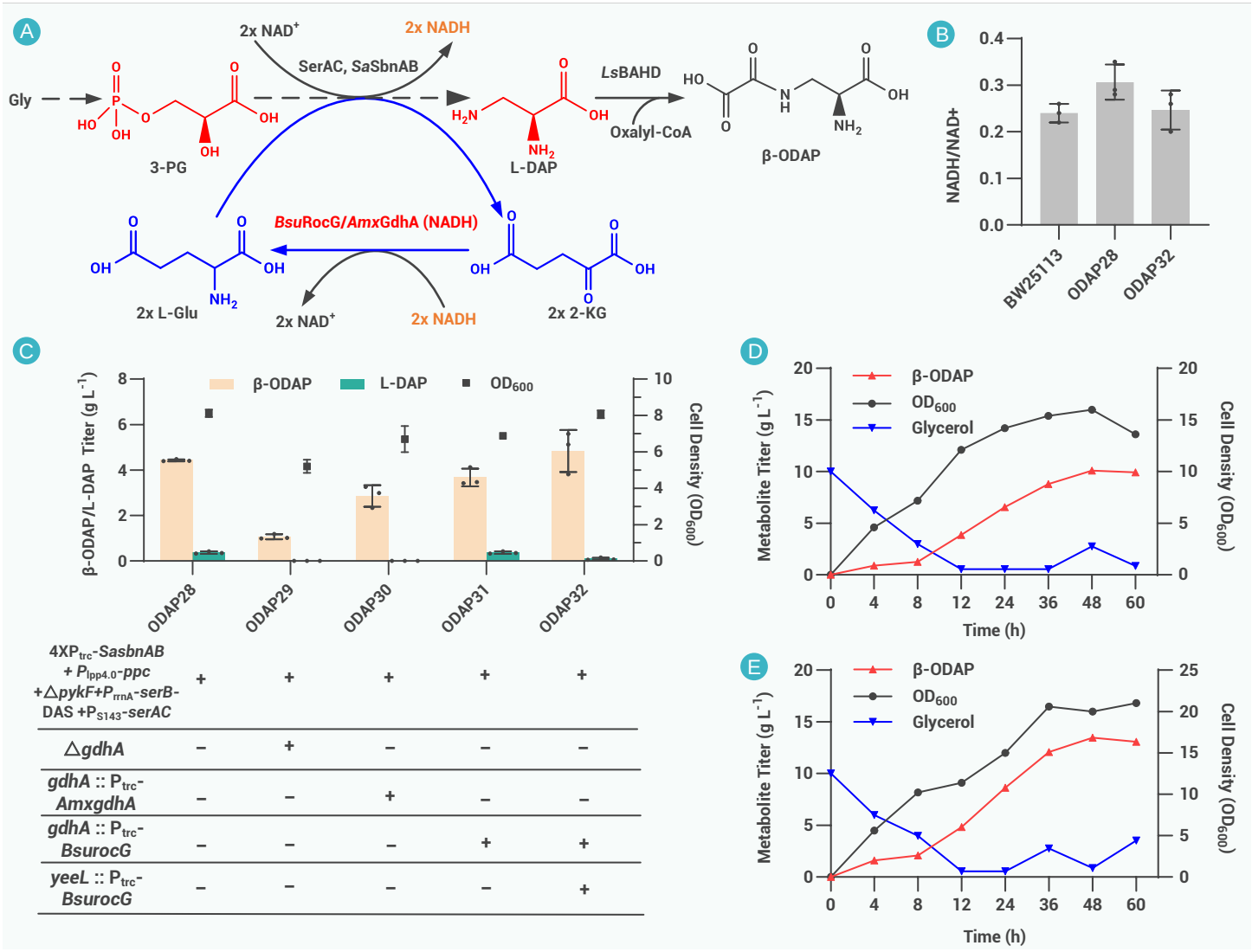

Figure 5. Construction of the cofactor cycling system and fed-batch fermentation (A) Schematic diagram of cofactor cycling. (B) Comparison of the NADH/NAD$^+$ ratio in BW25113, ODAP28, and ODAP32. (C) Improving β-ODAP titers by introducing NADH-dependent glutamate dehydrogenases *Amx*GdhA and *Bsu*RocG. (D) Fed-batch fermentation of ODAP28. (E) Fed-batch fermentation of ODAP32. The shake-flask fermentation data shown are the mean of n=3 biologically independent experiments and error bars represent standard deviation.

from weak to strong) were employed.[50] Among the 16 combinatorial circuits, five effectively produced higher fluorescence during growth and lower signal in stationary phase compared to the native P_{serB} (Figures 4C & S12). Considering that the high fluorescent peak and slow degradation rate exhibited by the rrnC-DAS combination circuit, we integrated other four circuits into the *yncI* locus. As shown in Figure 4D, strains ODAP22 (rrnA-DAS) and ODAP23 (rrnC-GSD) achieved β-ODAP titers of 3.81 g L^{-1} and 3.13 g L^{-1}, representing increases of 64.9% and 35.5% over ODAP21, along with growth recovery of 109.9% and 58.3%, respectively. The reduction of 2-HG to 3.5 mM in ODAP22 suggested restored TCA cycle activity (Figure 4G).

We next targeted the accumulation of toxic 2-HG, resulting from SerA overexpression, to further improve growth and production. Although the SerA mutant validated in the evolved strain effectively restored cell growth, it irreversibly reduced the supply of L-DAP. Therefore, we further attempted to convert 2-HG to 2-KG by overexpressing the endogenous FAD$^+$-dependent D-2-hydroxyglutarate dehydrogenase (YdiJ) from *E. coli*.[51] However, its overexpression adversely affected growth and β-ODAP synthesis, likely due to disrupted energy homeostasis (Figure S13). We therefore screened three stationary-phase promoters (SPPs; S60, S52, S143), which are repressed during the log phase and induced in the stationary phase, to dynamically activate the expression of *serA*.[52] Compared with the constitutive promoter P_{trc}, the SPPs showed lower expression during growth and higher expression in stationary phase (Figure 4E). We further replaced P_{trc} with SPPs to drive *serA* overexpression. Strains ODAP27 (S52) and ODAP28 (S143) increased in cell density by 7.5% and 12.2% and β-ODAP production by 13.6% and 16.3%, reaching titers of 4.33 g L^{-1} and 4.43 g L^{-1}, respectively (Figure 4F). Most notably, ODAP28 reduced 2-HG to trace levels (Figure 4G).

Reconstructing cofactor homeostasis to facilitate β-ODAP production

The β-ODAP pathway involves NADH generation by SerA and SbnB, while SerC and SbnA consume glutamate (Figure 1A). The NADH/NAD$^+$ ratio in ODAP28 was elevated by 29.2% compared to the wild type, suggesting cofactor imbalance limiting production (Figure 5B). To address this, we introduced NADH-dependent glutamate dehydrogenases to simultaneously supply glutamate and regenerate NAD$^+$ (Figure 5A).

Two candidates, *AmxgdhA* from *Amphibacillus xylanus*[53] and *BsurocG* from *Bacillus subtilis*[54], driven by P_{trc} promoter, were used to replace the native NADPH-dependent glutamate dehydrogenase gene *gdhA*. Compared with the *gdhA* knockout strain ODAP29, both candidates improved cell growth and β-ODAP production, with *BsurocG* achieving a higher titer of 3.67 g L^{-1} in ODAP31 (Figure 5C). However, ODAP31 still underperformed relative to the parent strain ODAP28. Additional genomic integration of P_{trc}-*BsurocG* (strain ODAP32) further increased β-ODAP titer to 4.84 g L^{-1}, 9.3% higher than ODAP28, while restoring cell growth to a similar level and reducing the NADH/NAD$^+$ ratio to 0.25 (Figures 5B-C). These results demonstrated that the introduction of the NADH-dependent glutamate dehydrogenase *Bsu*RocG

efficiently recycled cofactors and supplied glutamate, enhancing pathway balance and output.

Fed-batch fermentation in 3 L bioreactor

We scaled up production using fed-batch fermentation with controlled pH (7.0) and dissolved oxygen (25%). ODAP28 reached a maximum cell density (OD_{600}) of 16.0 at 48 h, producing 10.10 g L^{-1} β-ODAP with a yield of 0.29 g g^{-1} (Figure 5D). ODAP32 exhibited a similar profile, entering stationary phase at 36 h and reaching a maximum biomass cell density of 21.2 at 60 h, achieving a maximum titer of 13.46 g L^{-1} at 48 h with a yield of 0.32 g g^{-1} (Figure 5E). Compared to ODAP28, ODAP32 showed increases of 32.5% in biomass and 33.3% in β-ODAP titer, confirming that enhanced cofactor recycling and rebalanced cellular homeostasis significantly improved production performance.

DISCUSSION AND CONCLUSION

While microbial biosynthesis is gradually replacing plant extraction to meet the market demand for β-ODAP, its large-scale biotechnological production remains challenging. Compared with previous reports on β-ODAP biosynthesis,[42,43] our study achieved not only a substantially higher titer (13.46 g L^{-1}) and yield (0.32 g g^{-1}) but also uncovered and resolved a toxicity mechanism in the *L*-serine pathway. Earlier work focused primarily on optimizing precursor supply; here we demonstrate that systematic engineering must also address off-pathway metabolite toxicity caused by enzyme promiscuity.

A central challenge in constructing microbial cell factories is reconciling the trade-off between cell growth and product synthesis.[55] We achieved this balance through an integrated strategy. First, metabolic flux analysis identified the *L*-DAP branch as a bottleneck; multi-copy integration of *SasbnAB* and *serB* knockout redirected carbon from *L*-serine to *L*-DAP, but caused *L*-serine auxotrophy. Second, optimizing the AB module via modular pathway engineering and promoter engineering increased β-ODAP production by 223%. Third, we discovered that *serA* overexpression led to accumulation of the toxic byproduct 2-HG due to SerA promiscuity on α-ketoglutarate, explaining why *L*-serine/*L*-glycine supplementation only partially restored growth. Finally, we designed a growth-phase-dependent dual-dynamic circuit that gradually activated *serA* and progressively repressed *serB* as cells enter stationary phase, thereby uncoupling growth from production.

The toxicity of 2-HG to microbial growth has been documented.[56] Previous studies show that 2-HG inhibits α-ketoglutarate-dependent dioxygenases, interferes with DNA replication and repair, and disrupts cellular redox balance.[57–59] Consistent with these reports, exogenous 2-HG inhibited the growth of strain DAP6 in a dose-dependent manner (Figure 3I). Our metabolomic analysis revealed that in the evolved strain DAP-M19, 2-HG levels decreased by 78%, accompanied by increased glutamate and GABA, suggesting a redirection of carbon flux from the TCA cycle to amino acid metabolism. Notably, wild-type *E. coli* rapidly metabolized 20 mM 2-HG within 24 h (Figure S14), whereas engineered DAP6 accumulated 13 mM and grew poorly. We speculated that this differential tolerance arises from the stronger metabolic regulatory capacity of the wild-type strain, which may possess more robust detoxification systems. Future work should investigate these repair pathways for engineering.

Dual-dynamic regulation has been widely applied to address toxicity inhibition and metabolic competition. However, previous systems based on transcription factors or quorum sensing require the expression of exogenous regulatory proteins, which may impose an additional metabolic burden on the host.[36-37,60-61] In contrast, our circuit achieved reverse-coordinated, dual-target control using only growth-phase-dependent promoters combined with degrons, without exogenous inducers or heterologous regulatory proteins. Compared with previous representative studies on constructing cell factories for serine-pathway-derived metabolites (e.g., *L*-serine, *L*-tryptophan, and *L*-cysteine) by overexpressing *serA* or *serABC*,[23–26] our study not only demonstrated for the first time that *serA* overexpression leads to accumulation of the toxic byproduct 2-HG, which in turn inhibited cell growth, and also represented the first application of a bifunctional switch in the *L*-serine pathway to resolve toxicity inhibition and *L*-serine auxotrophy. This design was directly informed by the discovery of a specific toxicity target, demonstrating how mechanistic understanding can guide dynamic control architecture.

Cofactor imbalance was also addressed. The β-ODAP pathway generates NADH (via SerA and SbnB) and consumes glutamate (via SerC and SbnA). The NADH/NAD^+ ratio in ODAP28 was 29.2% higher than in the wild-type strain BW25113 (Figure 5B). Introducing NADH-dependent *Bsu*RocG reduced the ratio and improved β-ODAP titer by 9.3% in shake flasks (Figure 5C), but a much larger improvement (33.3%) was seen in fed-batch fermentation (Figure 5E). We attributed the modest shake-flask effect to oxygen and substrate limitations, which restrict NADH generation and glutamate availability, thereby underutilizing the engineered cofactor recycling system. This underscores the importance of evaluating cofactor engineering under industrially relevant conditions.

In summary, this study (i) identifies SerA-derived 2-HG as a hidden toxicity target, (ii) develops a reverse-coordinated dual-dynamic circuit to resolve auxotrophy and toxicity, and (iii) shows that cofactor homeostasis must be evaluated at production scale. The final strain ODAP32 achieved the highest reported β-ODAP titer and yield, making industrial production feasible. Future efforts may focus on engineering SerA to reduce its promiscuous activity and expanding the dual-dynamic strategy to other serine-derived chemicals.

REFERENCES

1. Gao J., Zuo Y., Xiao F., et al. (2022). Biosynthesis of catharanthine in engineered *Pichia pastoris*. *Nat. Synth.* **2**:231–242. DOI:10.1038/s44160-022-00205-2
2. Liang F., Xie Y., Zhang C., et al. (2025). Elucidation of the final steps in Taxol biosynthesis and its biotechnological production. *Nat. Synth.* **4**:1212–1222. DOI:10.1038/s44160-025-00800-z
3. Srinivasan P. and Smolke C. D. (2020). Biosynthesis of medicinal tropane alkaloids in yeast. *Nature* **585**:614–619. DOI:10.1038/s41586-020-2650-9
4. Lombe B. K., Zhou T., Kang G., et al. (2026). Biosynthesis of cinchona alkaloids. *Nature* **653**:306–314. DOI:10.1038/s41586-026-10227-x
5. Paddon C. J., Westfall P. J., Pitera D. J., et al. (2013). High-level semi-synthetic production of the potent antimalarial artemisinin. *Nature* **496**:528–532. DOI:10.1038/nature12051
6. Zhang J., Hansen L. G., Gudich O., et al. (2022). A microbial supply chain for production of the anti-cancer drug vinblastine. *Nature* **609**:341–347. DOI:10.1038/s41586-022-05157-3
7. Li X., Zhou Z., Li W., et al. (2022). Design of stable and self-regulated microbial consortia for chemical synthesis. *Nat. Commun.* **13**:1554. DOI:10.1038/s41467-022-29215-6
8. Bao T., Qian Y., Xin Y., et al. (2023). Engineering microbial division of labor for plastic upcycling. *Nat. Commun.* **14**:5712. DOI:10.1038/s41467-023-40777-x
9. Dahl R. H., Zhang F., Alonso-Gutierrez J., et al. (2013). Engineering dynamic pathway regulation using stress-response promoters. *Nat. Biotechnol.* **31**:1039–1046. DOI:10.1038/nbt.2689
10. Chen Z., Yu S., Liu J., et al. (2024). Concentration recognition-based auto-dynamic regulation system (CRUISE) enabling efficient production of higher alcohols. *Adv. Sci.* **11**:1–17. DOI:10.1002/advs.202310215
11. Zhang Y., Wei M., Zhao G., et al. (2021). Bioresource technology high-level production of L-homoserine using a non-induced, non-auxotrophic *Escherichia coli* chassis through metabolic engineering. *Bioresour. Technol.* **327**:124814. DOI:10.1016/j.biortech.2021.124814
12. Liu L., Li J., Gai Y., et al. (2023). Protein engineering and iterative multimodule optimization for vitamin B(6) production in *Escherichia coli*. *Nat. Commun.* **14**:5304. DOI:10.1038/s41467-023-40928-0
13. Fernández-Cabezón L., Rosich i Bosch B., Kozaeva E., et al. (2022). Dynamic flux regulation for high-titer anthranilate production by plasmid-free, conditionally-auxotrophic strains of *Pseudomonas putida*. *Metab. Eng.* **73**:11–25. DOI:10.1016/j.ymben.2022.05.008
14. Ma Y., Shang Y. and Stephanopoulos G. (2024). Engineering peroxisomal biosynthetic pathways for maximization of triterpene production in *Yarrowia lipolytica*. *Proc. Natl. Acad. Sci. USA* **121**:e2314798121. DOI:10.1073/pnas.2314798121
15. Zhou S., Yuan S. F., Nair P. H., et al. (2021). Development of a growth coupled and multi-layered dynamic regulation network balancing malonyl-CoA node to enhance (2S)-naringenin biosynthesis in *Escherichia coli*. *Metab. Eng.* **67**:41–52. DOI:10.1016/j.ymben.2021.05.007
16. Liang C., Zhang X., Wu J., et al. (2020). Dynamic control of toxic natural product biosynthesis by an artificial regulatory circuit. *Metab. Eng.* **57**:239–246. DOI:10.1016/j.ymben.2019.12.002
17. Pitera D. J., Paddon C. J., Newman J. D., et al. (2007). Balancing a heterologous mevalonate pathway for improved isoprenoid production in *Escherichia coli*. *Metab. Eng.* **9**:193–207. DOI:10.1016/j.ymben.2006.11.002
18. Dueber J. E., Wu G. C., Malmirchegini G. R., et al. (2009). Synthetic protein scaffolds provide modular control over metabolic flux. *Nat. Biotechnol.* **27**:753–759. DOI:10.1038/nbt.1557
19. Peracchi A. (2018). The limits of enzyme specificity and the evolution of metabolism. *Trends Biochem. Sci.* **43**:984–996. DOI:10.1016/j.tibs.2018.09.015
20. Niehaus T. D. and Hillmann K. B. (2020). Enzyme promiscuity, metabolite damage, and metabolite damage control systems of the tricarboxylic acid cycle. *FEBS J.*

287:1343–1358. DOI:10.1111/febs.15284
21. Sun J., Jeffryes J. G., Henry C. S., et al. (2017). Metabolite damage and repair in metabolic engineering design. *Metab. Eng.* **44**:150–159. DOI:10.1016/j.ymben.2017.10.006
22. Linster C. L., Van Schaftingen E. and Hanson A. D. (2013). Metabolite damage and its repair or pre-emption. *Nat. Chem. Biol.* **9**:72–80. DOI:10.1038/nchembio.1141
23. Hou M., Gao S., Wu J., et al. (2025). Metabolic engineering of *Escherichia coli* to enhance L-tryptophan biosynthesis. *Syst. Microbiol. Biom.* **5**:622–634. DOI:10.1007/s43393-025-00338-3
24. Gu P., Yang F., Su T., et al. (2014). Construction of an L-serine producing *Escherichia coli* via metabolic engineering. *J. Ind. Microbiol. Biotechnol.* **41**:1443–1450. DOI:10.1007/s10295-014-1476-6
25. Zhang X., Zhang D., Zhu J., et al. (2019). High-yield production of l-serine from glycerol by engineered *Escherichia coli*. *J. Ind. Microbiol. Biotechnol.* **46**:221–230. DOI:10.1007/s10295-018-2113-6
26. Liu H., Fang G., Wu H., et al. (2018). L-cysteine production in *Escherichia coli* based on rational metabolic engineering and modular strategy. *Biotechnol. J.* **13**:1–6. DOI:10.1002/biot.201700695
27. Bankole O. E., Verma D. K., Chávez González M. L., et al. (2022). Recent trends and technical advancements in biosensors and their emerging applications in food and bioscience. *Food Biosci.* **47**:101695. DOI:10.1016/j.fbio.2022.101695
28. Zou Y., Zhang J., Wang J., et al. (2024). A self-regulated network for dynamically balancing multiple precursors in complex biosynthetic pathways. *Metab. Eng.* **82**:69–78. DOI:10.1016/j.ymben.2024.02.001
29. Ream M. and Prather K. L. J. (2024). Engineered autonomous dynamic regulation of metabolic flux. *Nat. Rev. Bioeng.* **2**:233–243. DOI:10.1038/s44222-023-00140-7
30. Yang Y., Lin Y., Wang J., et al. (2018). Sensor-regulator and RNAi based bifunctional dynamic control network for engineered microbial synthesis. *Nat. Commun.* **9**:1–10. DOI:10.1038/s41467-018-05466-0
31. Song C., Luan J., Cui Q., et al. (2019). Enhanced heterologous spinosad production from a 79-kb synthetic multioperon assembly. *ACS Synth. Biol.* **8**:137–147. DOI:10.1021/acssynbio.8b00402
32. Ge C., Yu Z., Sheng H., et al. (2022). Redesigning regulatory components of quorum-sensing system for diverse metabolic control. *Nat. Commun.* **13**:1–12. DOI:10.1038/s41467-022-29933-x
33. Doong S. J., Gupta A. and Prather K. L. J. (2018). Layered dynamic regulation for improving metabolic pathway productivity in *Escherichia coli*. *Proc. Natl. Acad. Sci. USA* **115**:2964–2969. DOI:10.1073/pnas.1716920115
34. Stella R. G., Gertzen C. G. W., Smits S. H. J., et al. (2021). Biosensor-based growth-coupling and spatial separation as an evolution strategy to improve small molecule production of *Corynebacterium glutamicum*. *Metab. Eng.* **68**:162–173. DOI:10.1016/j.ymben.2021.10.003
35. Lu L., Wang X., Wang T., et al. (2024). A bacterial platform for producing aromatic esters from glycerol. *Nat. Chem. Eng.* **1**:751–764. DOI:10.1038/s44286-024-00148-9
36. Hou J., Gao C., Guo L., et al. (2020). Rewiring carbon flux in *Escherichia coli* using a bifunctional molecular switch. *Metab. Eng.* **61**:47–57. DOI:10.1016/j.ymben.2020.05.004
37. Wei L., Zhao J., Wang Y., et al. (2022). Engineering of *Corynebacterium glutamicum* for high-level γ-aminobutyric acid production from glycerol by dynamic metabolic control. *Metab. Eng.* **69**:134–146. DOI:10.1016/j.ymben.2021.11.010
38. Lee J. M., Hammarén H. M., Savitski M. M., et al. (2023). Control of protein stability by post-translational modifications. *Nat. Commun.* **14**:1–16. DOI:10.1038/s41467-023-35795-8
39. Xu P., Li L., Zhang F., et al. (2014). Improving fatty acids production by engineering dynamic pathway regulation and metabolic control. *Proc. Natl. Acad. Sci. USA* **111**:11299–11304. DOI:10.1073/pnas.1406401111
40. Huang L., Shi H., Gao B., et al. (2014). Decichine enhances hemostasis of activated platelets via AMPA receptors. *Thromb. Res.* **133**:848–854. DOI:10.1016/j.thromres.2014.02.009
41. Li J., Qiu P., Wang S., et al. (2019). β-N-Oxalyl-L-α,β-diaminopropionic acid from *Panax notoginseng* plays a major role in the treatment of type 2 diabetic nephropathy. *Biomed. Pharmacother.* **114**:108801. DOI:10.1016/j.biopha.2019.108801
42. Huang D., Wang X., Liu W., et al. (2023). Remodeling metabolism of *Corynebacterium glutamicum* for high-level dencichine production. *Bioresour. Technol.* **388**:129800. DOI:10.1016/j.biortech.2023.129800
43. Li W., Zhou Z., Li X., et al. (2022). Biosynthesis of plant hemostatic dencichine in *Escherichia coli*. *Nat. Commun.* **13**:5492. DOI:10.1038/s41467-022-33255-3
44. Jiang Y., Chen B., Duan C., et al. (2015). Multigene editing in the *Escherichia coli* genome via the CRISPR-Cas9 system. *Appl. Environ. Microbiol.* **81**:2506–2514. DOI:10.1128/AEM.04023-14
45. Edwards A., Njaci I., Sarkar A., et al. (2023). Genomics and biochemical analyses reveal a metabolon key to β-L-ODAP biosynthesis in *Lathyrus sativus*. *Nat. Commun.* **14**:5199. DOI:10.1038/s41467-023-36503-2
46. Kim J. and Copley S. D. (2012). Inhibitory cross-talk upon introduction of a new metabolic pathway into an existing metabolic network. *Proc. Natl. Acad. Sci. USA* **109**:E2856–64. DOI:10.1073/pnas.1208509109
47. Kim J., Kershner J. P., Novikov Y., et al. (2010). Three serendipitous pathways in *E. coli* can bypass a block in pyridoxal-5'-phosphate synthesis. *Mol. Syst. Biol.* **6**:1–13. DOI: 10.1038/msb.2010.88.
48. Zhao G. and Winkler M. E. (1996). A novel α-ketoglutarate reductase activity of the sera-encoded 3-phosphoglycerate dehydrogenase of *Escherichia coli* K-12 and its possible implications for human 2-hydroxyglutaric aciduria. *J. Bacteriol.* **178**:232–239. DOI:10.1128/jb.178.1.232-239.1996
49. Lemke J. J., Sanchez-Vazquez P., Burgos H. L., et al. (2011). Direct regulation of *Escherichia coli* ribosomal protein promoters by the transcription factors ppGpp and DksA. *Proc. Natl. Acad. Sci. USA* **108**:5712–5717. DOI:10.1073/pnas.1019383108
50. McGinness K. E., Baker T. A. and Sauer R. T. (2006). Engineering controllable protein degradation. *Mol. Cell* **22**:701–707. DOI:10.1016/j.molcel.2006.04.027
51. Samsonov V. V., Kuznetsova A. A., Rostova J. G., et al. (2022). Revealing a new family of D-2-hydroxyglutarate dehydrogenases in *Escherichia coli* and *Pantoea ananatis* encoded by *ydiJ*. *Microorganisms*. **10**:1766. DOI:10.3390/microorganisms10091766
52. Miksch G., Bettenworth F., Friehs K., et al. (2005). The sequence upstream of the -10 consensus sequence modulates the strength and induction time of stationary-phase promoters in *Escherichia coli*. *Appl. Microbiol. Biotechnol.* **69**:312–320. DOI:10.1007/s00253-005-0016-8
53. Jahns T. (1996). Unusually stable NAD-specific glutamate dehydrogenase from the alkaliphile *Amphibacillus xylanus*. *Anton. Leeuw. Int. J. G.* **70**:89–95. DOI:10.1007/BF00393573
54. Piao X., Wang L., Lin B., et al. (2019). Metabolic engineering of *Escherichia coli* for production of L-aspartate and its derivative β-alanine with high stoichiometric yield. *Metab. Eng.* **54**:244–254. DOI:10.1016/j.ymben.2019.04.012
55. Liu L., Ding D., Wang H., et al. (2025). Balancing cell growth and product synthesis for efficient microbial cell factories. *Adv. Sci.* **12**:e10649. DOI:10.1002/advs.202510649
56. Xiao D., Zhang W., Guo X., et al. (2021). A d-2-hydroxyglutarate biosensor based on specific transcriptional regulator DhdR. *Nat. Commun.* **12**:1–14. DOI:10.1038/s41467-021-27357-7
57. Liu Y., Kang Z., Zhang W., et al. (2024). Metabolic functions of misunderstood D-2-hydroxyglutarate. *Innov. Life* **2**:100101. DOI:10.59717/j.xinn-life.2024.100101
58. Kang Z., Zhang M., Gao K., et al. (2021). An l-2-hydroxyglutarate biosensor based on specific transcriptional regulator LhgR. *Nat. Commun.* **12**:3619. DOI:10.1038/s41467-021-23723-7
59. Ye D., Guan K. and Xiong Y. (2018). Metabolism, activity, and targeting of D- and L-2-hydroxyglutarates. *Trends in Cancer* **4**:151–165. DOI:10.1016/j.trecan.2017.12.005
60. Dinh C. V. and Prather K. L. J. (2019). Development of an autonomous and bifunctional quorum-sensing circuit for metabolic flux control in engineered *Escherichia coli*. *Proc. Natl. Acad. Sci. USA* **116**:25562–25568. DOI:10.1073/pnas.1911144116
61. Yuan S., Xu C., Jin M., et al. (2025). Stress-driven dynamic regulation of multiple genes to reduce accumulation of toxic aldehydes. *Metab. Eng.* **90**:129–140. DOI:10.1016/j.ymben.2025.03.009

FUNDING AND ACKNOWLEDGMENTS

This work was supported by the National Key Research and Development Program of China (2025YFA0921800), the National Natural Science Foundation of China (22322802, 32271488). The funders had no role in study design, data collection and analysis, decision to publish, or preparation of the manuscript.

AUTHOR CONTRIBUTIONS

Y.Z., XX.S. and Q.Y. designed the experiments. Y.Z. performed the experiments. J.Wu., J.Y., Y.T. and C.X helped design experiments. Y.Z. and XX.S. analyzed the data and wrote the manuscript. XX.S., Q.Y., XL.S., J.Wang. and Y.Y. participated in the discussion and revision of the manuscript. All authors contributed to the manuscript and approved the final version.

DECLARATION OF INTERESTS

The authors declare no competing interests.

ETHICAL STATEMENT AND PATIENT CONSENT

Not applicable.

DATA AND CODE AVAILABILITY

Data supporting the findings of this work are available within the article and its Supplemental Information file.

SUPPLEMENTAL INFORMATION

It can be found online at https://doi.org/10.59717/j.xinn-life.2026.100242.